

## Vertical drying of a suspension of sticks: Monte Carlo simulation for continuous two-dimensional problem

Nikolai I. Lebovka,<sup>1,2,\*</sup> Yuri Yu. Tarasevich,<sup>3,†</sup> and Nikolai V. Vygornitskii<sup>1</sup>

<sup>1</sup>*Department of Physical Chemistry of Disperse Minerals, F. D. Ovcharenko Institute of Biocolloidal Chemistry, NAS of Ukraine, Kiev, Ukraine, 03142*

<sup>2</sup>*Department of Physics, Taras Shevchenko Kiev National University, Kiev, Ukraine, 01033*

<sup>3</sup>*Laboratory of Mathematical Modeling, Astrakhan State University, Astrakhan, Russia, 414056*



(Received 30 October 2017; published 21 February 2018)

The vertical drying of a two-dimensional colloidal film containing zero-thickness sticks (lines) was studied by means of kinetic Monte Carlo (MC) simulations. The continuous two-dimensional problem for both the positions and orientations was considered. The initial state before drying was produced using a model of random sequential adsorption with isotropic orientations of the sticks. During the evaporation, an upper interface falls with a linear velocity in the vertical direction, and the sticks undergo translational and rotational Brownian motions. The MC simulations were run at different initial number concentrations (the numbers of sticks per unit area),  $p_i$ , and solvent evaporation rates,  $u$ . For completely dried films, the spatial distributions of the sticks, the order parameters, and the electrical conductivities of the films in both the horizontal,  $x$ , and vertical,  $y$ , directions were examined. Significant evaporation-driven self-assembly and stratification of the sticks in the vertical direction was observed. The extent of stratification increased with increasing values of  $u$ . The anisotropy of the electrical conductivity of the film can be finely regulated by changes in the values of  $p_i$  and  $u$ .

DOI: [10.1103/PhysRevE.97.022136](https://doi.org/10.1103/PhysRevE.97.022136)

### I. INTRODUCTION

The technique of vertical drying of suspensions is frequently applied for producing colloidal crystals with many intriguing properties [1]. However, this technique requires precise control of the drying conditions, including the concentration of particles, their size distribution, the temperature, humidity, drying time, etc. [2]. Moreover, the drying process can be complicated by the formation of a skin barrier at the top of the drying film and the emergence of irregular structures and of vertical segregation as well as the development of evaporation-induced self-assembly [3,4].

Uniformity in particle arrangement during vertical drying is controlled by solvent evaporation, sedimentation processes, and diffusion of the particles. It is useful to introduce the so-called Péclet number that is the ratio of the characteristic diffusive ( $\tau_D$ ) and evaporation ( $\tau_E$ ) times,  $Pe = \tau_D/\tau_E$ . These times can be defined as  $\tau_D = H^2/D$  and  $\tau_E = H/u$ , where  $H$  is the initial thickness of the film in the vertical direction,  $D$  is a diffusion constant for the particle, and  $u$  is the rate of evaporation. Uniformity in particle arrangement is expected at  $Pe = uH/D \ll 1$ , i.e., at small  $u$  or high  $D$ , whereas in the opposite case, for large Péclet numbers, a spatial gradient is typically observed in the density profile [3].

Different regimes of vertical drying of suspensions filled with spherical and anisotropic colloidal particles have been extensively studied in experimental works (for a review see Ref. [3]). Experimental studies of the drying of colloidal

suspensions filled with rodlike particles (with aspect ratios ranging from 4 to 15) revealed parallel orientation of the rods in several layers close to the contact line [5]. Special interest has been paid to the behaviors of dried films of highly anisotropic carbon nanotubes (for a review, see Ref. [6]). These transparent and electrically conductive films present particular interest for the production of electrodes for super-capacitors, thin film transistors, and fuel cells.

However, it is hard, experimentally, to determine many of the properties of the final dried films and the density profiles of the particles through those films [3]. Computation approaches can therefore provide valuable information, helpful for understanding the mechanisms of vertical drying and for determining the properties of the eventual dried films.

For spherical particles, Brownian, Langevin dynamics, and kinetic Monte Carlo (MC) simulations have been applied to study the vertical drying of one-, two-, three-component and polydisperse three-dimensional (3D) colloidal suspensions [7–13]. For binary systems, either random spatial distribution or heterocoagulation were observed in dependence on differences in the surface charges of constituents [7]. The formation of ordered hexagonal or tetragonal domains and random packing at low and high evaporation rates, respectively, has also been observed [8]. The simulation models have also included the effects of inter-particle and particle-surface interactions and size polydispersity [9,10]. At a relatively low evaporation rate, films with low porosity and low surface roughness were formed [10]. For polydispersed systems a dynamic stratification by size in the drying films was noted, with a layer of larger particles at the bottom and one of smaller particles on the top [11]. A segregation mechanism for this has been explained through the so-called colloidal diffusiophoresis effect related to the

\*lebovka@gmail.com

†tarasevich@asu.edu.ru

presence of a colloidal osmotic pressure gradient developed during the drying. Stratification has also been observed for ternary and polydisperse mixtures [12]. The proposed model predicted a power-law dependence of the phoretic velocity on particle size. Kinetic MC simulations of vertical drying using two-dimensional (2D) models at various Péclet numbers have been performed [13]. At  $Pe \gg 1$ , the particles accumulated at the top of the layer whereas, at  $Pe \ll 1$ , significant aggregation of particles in the bulk colloid could be observed and the resulting film structure became highly porous. Vertical drying has also been studied using a hybrid simulation method based on a cell model [14]. Various cases of hard or soft particles, different interaction potentials, and different drying conditions were tested. A linear increase of concentration gradient with increased value of  $Pe$ , was observed although this effect was partially hindered in systems with strong repulsive interaction between the particles.

Computational studies of vertical drying have been performed much less frequently for particles with anisotropic shape. Recently, the vertical drying of 2D colloidal films filled with anisotropic particles by means of a kinetic MC simulation has been studied [15]. The oversimplified lattice problem in which the particles are represented by linear  $k$ -mers (particles occupying  $k$  adjacent sites) was addressed. The initial state of the film before drying was produced using a model of random sequential adsorption (RSA) on a square lattice, with only two restricted orientations along the lattice axes being allowed. During the drying, the upper interface falls with a linear velocity in the vertical direction, and the particles undergo translational Brownian motion. For completely dried films, the density profiles of the particles and the electrical conductivity in both directions were calculated. The simulations revealed significant evaporation-driven self-assembly together with orientation stratification of the particles with different orientations. It is well known that molecular dynamics simulation can offer more precise description of behavior in compare with kinetic Monte Carlo simulation (see, e.g., Ref. [16]). Nevertheless, such the simulation is extremely time-consuming.

Note that studies of self-assembly and phase behavior in equilibrium colloidal systems filled with anisotropic particles have a fairly long history and have attracted a great deal of attention for many years. The existence of a nematic phase was firstly predicted by Onsager for a 3D continuous systems of very long rods (needles) that interact only through the excluded volume effect [17]. The theory predicted a transition to this nematic phase with strong orientation ordering at some critical number density,  $\rho_n \approx 4.19$ . Moreover, the coexisting isotropic and nematic phases between  $\rho_i \approx 3.29$  and  $\rho_n$  were also predicted. Several extended approaches have subsequently been proposed, and they all agree with Onsager's estimations in the limit of low densities for sufficiently long rods [18–21].

A reduction in spatial dimensionality from 3D to 2D influences the nature of the ordered phases. The 2D version of the Onsager theory for a system of needles predicted a continuous nematic-isotropic (N-I) transition at a critical density of  $\rho_i = 3\pi/2 \approx 4.7$  [22]. The 2D equivalent of the Maier-Saupe theory predicted a continuous N-I transition [23]. A transition from disordered to a partially ordered phase was also confirmed using the MC technique for particles confined

to the sites of a triangular lattice [23]. The MC simulations demonstrated the presence of N-I transitions as particle density was increased [24,25]. It was shown that for the 2D systems, only a quasi-long-range order with algebraic decay of the order-parameter correlation function can be realized. At relatively small densities  $\rho < 7$  the ordered phase became absolutely unstable with respect to disclination unbinding, but at  $\rho \geq \rho_n \approx 7.25$ , a 2D nematic phase with algebraic order appeared. The phase behavior of hard ellipses with an aspect ratio of  $k = 6$  has been studied using MC simulations [26]. The system exhibited two first-order phase transitions: a solid-nematic one (at high density) and an N-I one (at a density 1.5 times smaller). These transitions were attributed to geometrical factors. No evidence for a first order N-I transition was found using MC simulation of hard rods [24]. The nematic phase demonstrated algebraic order (quasi-long-range order) and the occurrence of a disclination-unbinding transition of the Kosterlitz-Thouless (KT) type has been suggested. A mean field model has predicted nematic, columnar, and crystalline order in dense systems of parallel hard rods in 2D systems [27]. A density functional theory for the N-I transition in a 2D system of rods has been developed and it predicts a continuous (second order) N-I transition [28]. MC simulations have been applied to study the phase behavior of continuous 2D fluid systems with spherocylinders (tapered cylinders) [25]. At high density for long rods with high aspect ratios  $k \gtrsim 7$ , a 2D nematic phase of the KT type occurred. Shorter rods exhibited a melting transition to an isotropically arranged phase dominated by chains of particles that aligned side-by-side. An off-lattice model of liquid crystals has been proposed and applied to description of N-I transitions [29].

For nonequilibrium 2D systems obtained using the RSA process, further self-assembly is possible owing to deposition-evaporation processes or to the diffusion motion of the anisotropic particles. Several problems related to such types of self-assembly of  $k$ -mers have previously been discussed [30–36]. Dynamic MC simulations using a deposition-evaporation algorithm for simulation of the dynamic equilibrium of  $k$ -mers on square lattices have been applied [30]. For long  $k$ -mers ( $k \geq 7$ ), two entropy-driven transitions as a function of density,  $\rho$ , were revealed: first, from a low-density isotropic phase to a nematic phase with an intermediate density at  $\rho_{in}$ , and, second, from the nematic phase to a high-density disordered phase at  $\rho_{nd}$ . A lattice-gas model approach has been applied to study the phase diagram of self-assembled  $k$ -mers on square lattices [31]. It has been observed that an irreversible RSA process leads to an intermediate state with purely local orientational order, while, in the equilibrium model, the nematic order can be stabilized for sufficiently long  $k$ -mers [34,35]. It was also demonstrated that equilibration of the RSA structure by Brownian diffusion of the particles on a square lattice resulted in the segregation of clusters of  $k$ -mers with different orientations [36].

Therefore, self-assembly in colloidal suspensions filled with anisotropic particles is fairly typical for both 3D and 2D systems, and it can develop in different manners for continuous and lattice problems, depending on the initial state of the system and the equilibration procedure applied. This self-assembly can be even more complicated during the vertical drying processes. Nevertheless, in spite of great interest in the

problem, it has never previously been discussed for the more advanced off-lattice model taking account of the Brownian diffusion of sticks during vertical drying.

This paper analyzes the self-assembly in 2D colloidal suspensions of sticks during vertical drying. It has been assumed that the sticks are infinitely thin, and kinetic MC simulations have been applied. The initial state was produced using RSA with isotropic orientations of the sticks, after which the drying was started and the sticks were allowed to undergo both translational and the rotational diffusion. The kinetics of the changes of structure and the electrical conductivity in the horizontal ( $x$ ) and vertical ( $y$ ) directions have been analyzed.

The rest of the paper is constructed as follows. In Sec. II the technical details of the simulations are described, all necessary quantities are defined, and some test results are given. Section III presents our principal findings. Section IV summarizes the main results.

## II. COMPUTATIONAL MODEL

The RSA model was used to produce a distribution of sticks with a desirable initial number density  $\rho_i$  [37]. Sticks with length of  $l_s$  and zero thickness,  $d_s = 0$  (i.e., with infinite aspect ratio,  $k = l_s/d_s = \infty$ ), were deposited on a plane randomly (both their positions and orientations were random) and sequentially, while their overlapping with previously placed particles was forbidden. The kinetics of RSA deposition for such systems has been studied in detail [38–40]. Note that since the sticks have zero thickness, the jamming number density  $\rho_j$  is never reached for this model. However, for sticks with large but finite aspect ratios  $k$ , the number density is finite and increases with  $k$  as  $\rho_j \sim k^{0.8}$  [40,41].

The length of the system was  $L$  along the horizontal  $x$  direction and initial height was  $H_i$  along the vertical  $y$  direction. In the present work, all calculations were performed using  $L = H_i = 32l_s$ . Our choice is based on scaling analysis. Example of scaling analysis is presented in Appendix B. In our computations of vertical drying, periodic boundary conditions were applied along the  $x$  axis. A zero flux boundary condition was applied at the bottom border (liquid-substrate interface). The upper border (liquid-vapor interface) moves down due to evaporation, and this interface is impenetrable for the sticks. An isotropic initial orientation of the sticks was assumed.

The simulation of the vertical drying procedure assumed simultaneous Brownian motion of the sticks and a downward movement of the vapor-liquid interface. The Brownian diffusion of sticks was simulated using the kinetic MC procedure. At each step, an arbitrary stick was randomly chosen. The 2D translational and rotational diffusion motions were taken into consideration. For 2D translation,  $D_t$ , and rotational,  $D_r$ , the diffusion coefficients, the formulas for long,  $k \gg 1$ , rodlike particles were used [42],

$$D_t = \frac{3k_B T [\ln(k) + \gamma_t]}{8\pi\eta l_s}, \quad D_r = \frac{k_B T [\ln(k) + \gamma_r]}{\pi\eta l_s^3}, \quad (1)$$

where  $k_B T$  is the thermal energy,  $\eta$  is the viscosity of surrounding liquid, and  $\gamma_r \approx 0.219$  and  $\gamma_t \approx -0.447$  are the end correction coefficients [43–45].

The ratio of the mean-square rotation  $\langle \Delta\theta^2 \rangle$  and mean-square displacement in the center of mass position  $\langle \Delta l^2 \rangle$  over

the time  $\Delta t$  was calculated as

$$\frac{\langle \Delta\theta^2 \rangle}{\langle \Delta l^2 \rangle} = \frac{2D_r \Delta t}{4D_t \Delta t} \approx 4. \quad (2)$$

In each MC step, displacement in an arbitrary direction by a value of  $\sqrt{\langle \Delta l^2 \rangle}$  or rotation by value a of  $\sqrt{\langle \Delta\theta^2 \rangle}$  with probabilities proportional to the corresponding diffusion coefficients  $D_t$  and  $D_r$ , respectively, were attempted. The value of maximum MC displacement  $\sqrt{\langle \Delta l^2 \rangle}$  was chosen to be small enough ( $\alpha = \sqrt{\langle \Delta l^2 \rangle}/l \approx 0.1 - 0.05$ ) in order to obtain satisfactory acceptance of the MC displacement [46]. Each one time MC step,  $\Delta t_{MC}$ , corresponds to an attempted displacement and rotation of the total number of sticks in the system. The value of  $\Delta t_{MC}$  corresponds to the real time  $\tau_B \alpha^2$ , where

$$\tau_B = l_s^2/(4D_t) \quad (3)$$

is the Brownian time. Time counting was started from the value of  $t_{MC} = 1$ , being the initial moment (before drying and diffusion), and the total duration of the simulation was typically  $10^6 - 10^7$  MC time units.

As the interface moves downward, the sticks tend to accumulate below it. Some sticks become trapped at the interface because of the effects of surface tension, and these are unable to move above the interface. Below the interface the sticks can diffuse normally.

For characterization of the processes, some parameters were calculated during the course of the simulation:

- (1) The relative height of the film,  $h = H/H_i$
- (2) The running number density,  $\rho$
- (3) The mean order parameter of the system  $S$
- (4) The distributions of local number density,  $\rho(y)$ , and local order parameter  $S(y)$  along the vertical axis  $y$
- (5) The electrical conductivities along the  $x$  and  $y$  axes.

The mean order parameter was calculated as

$$S = \frac{1}{N} \sum_i (2 \cos^2 \theta_i - 1), \quad (4)$$

where  $\theta_i$  is the angle between the axis of the  $i$ th stick and the horizontal axis  $x$ , and the summation runs over all  $N$  particles in the system.

To calculate the distributions of local number density,  $\rho(y)$ , and local order parameter,  $S(y)$ , along the vertical axis  $y$ , the film was divided into regular strips with width of  $\Delta y = H/32$ . In calculations of the density and order parameter profiles, those sticks with coordinates of a center of mass inside the given strip,  $y \leq y_i < y + \Delta y$ , were taken into account (Fig. 1).

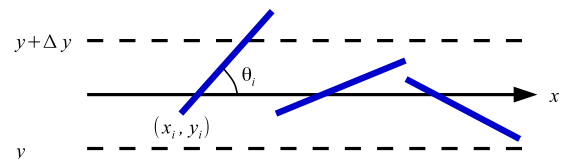


FIG. 1. To the calculation of the distributions of local number density,  $\rho(y)$ , and local order parameter,  $S(y)$ , along the vertical axis  $y$ . Here  $y_i$  is the vertical coordinate of the center of the stick,  $\Delta y = H/32$  is the width of the strip,  $H$  is the running height of the film,  $\theta_i$  is the angle between axis of the stick and the horizontal axis  $x$ .

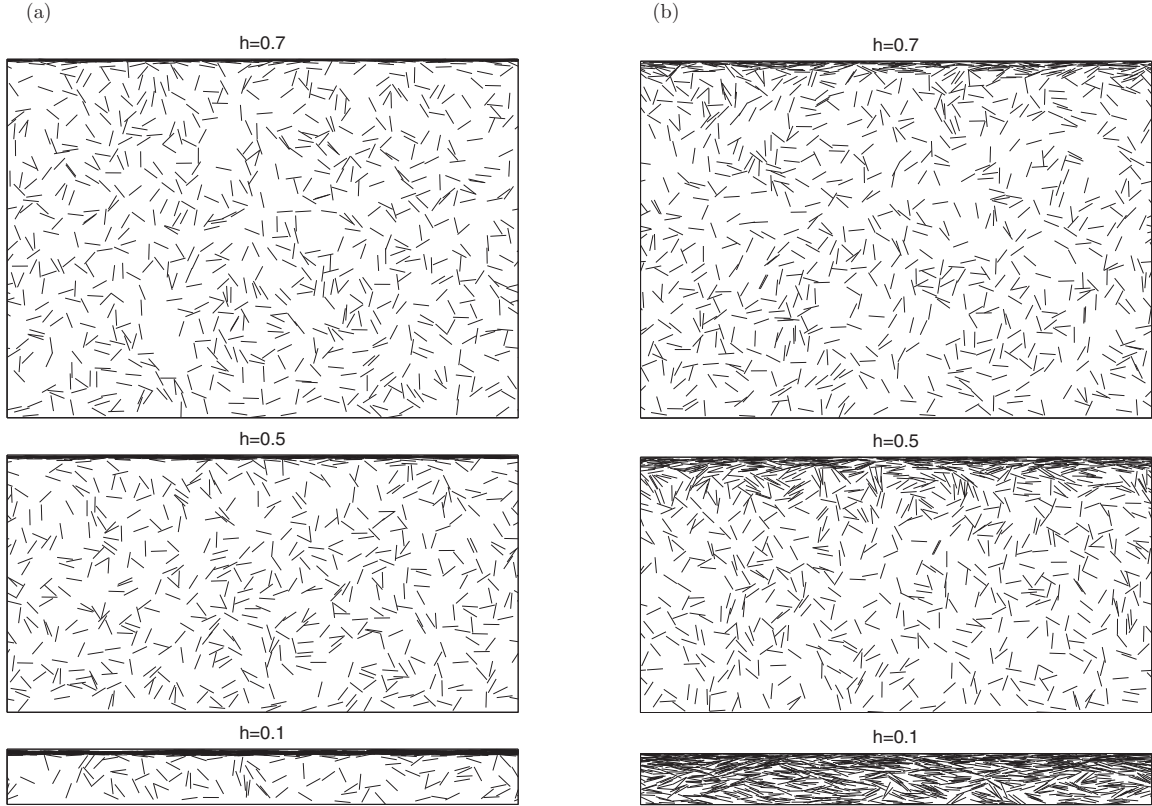


FIG. 2. Evolution of drying patterns at different values of the relative height of the film,  $h$ , for a constant drying rate,  $u = 10^{-3}$  [ $\rho_c = \infty$  in Eq. (5)] (a), and for a variable drying rate [ $\rho_c = 7$  in Eq. (5)] (b). The initial concentration of sticks was  $\rho_i = 1.0$ .

For calculation of the electrical conductivity, the discretization scheme of the problem with a supporting square lattice of size  $m \times m$  ( $m = 256, 512, \text{ and } 1024$ ) was used. The sites of the supporting lattice covered by sticks were assumed as conducting and the others were assumed as insulating. See Appendix A for details. The Frank-Lobb algorithm was applied to evaluate the electrical conductivity [47]. We put  $\sigma_i = 1$  and  $\sigma_c = 10^6$  in arbitrary units for the conductivities of insulating and conducting sites, respectively. In our calculations, the two conducting buses were applied to the opposite borders of the lattice, and electrical conductivity was calculated between these buses in the horizontal,  $\sigma_x$  and vertical  $\sigma_y$  directions (see Refs. [15,36] for the details).

Note that our assumption of the constancy of the drying rate is a rather rough approximation. The formation of a more dense layer (crust or barrier) near the upper vapor-liquid interface can result in a restriction of the evaporation of the liquid and a decreasing value of  $u$ . To account for this effect, the maximum number density  $\rho_m$  in the crust was calculated, and a running value of the drying rate  $u$  was evaluated using an exponential approximation,

$$u = u_i \exp(-\rho_m/\rho_c), \quad (5)$$

where  $u_i$  is the initial drying rate, and  $\rho_c$  is a parameter (characteristic density) that controls the effect of the crust on the drying rate.

This oversimplified approximation was used only for qualitative estimations of the barrier properties of a dense layer on the drying rate. In the general case, the barrier properties

can depend on details of the structure, density, and thickness of the layer of sticks oriented along the evaporating interface (see Ref. [48] and references therein for the details). The transition from the isotropic to the ordered nematic phase was observed at  $\rho \approx 7$  [24,25]. Enhancement of the barrier properties can be assumed in the nematic phase structure, and, in this investigation, we put  $\rho_c = 7$ .

Figure 2 presents examples of the drying patterns at different values of the relative height of the film,  $h = H/H_i$ . The cases of

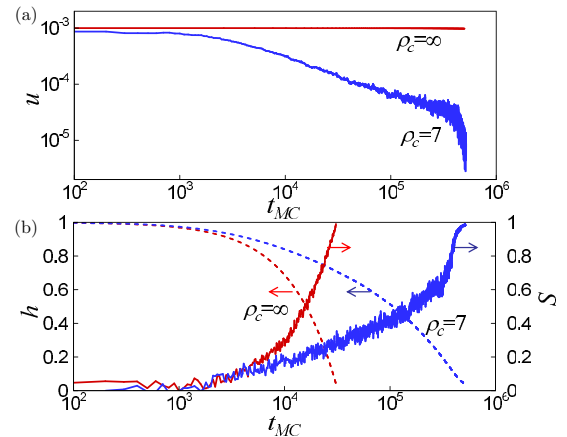


FIG. 3. Drying rate,  $u$  (a), relative height of the film,  $h$ , and average order parameter,  $S$  (b), for constant and variable drying rates vs MC steps. The initial concentration of sticks was  $\rho_i = 1.0$ .

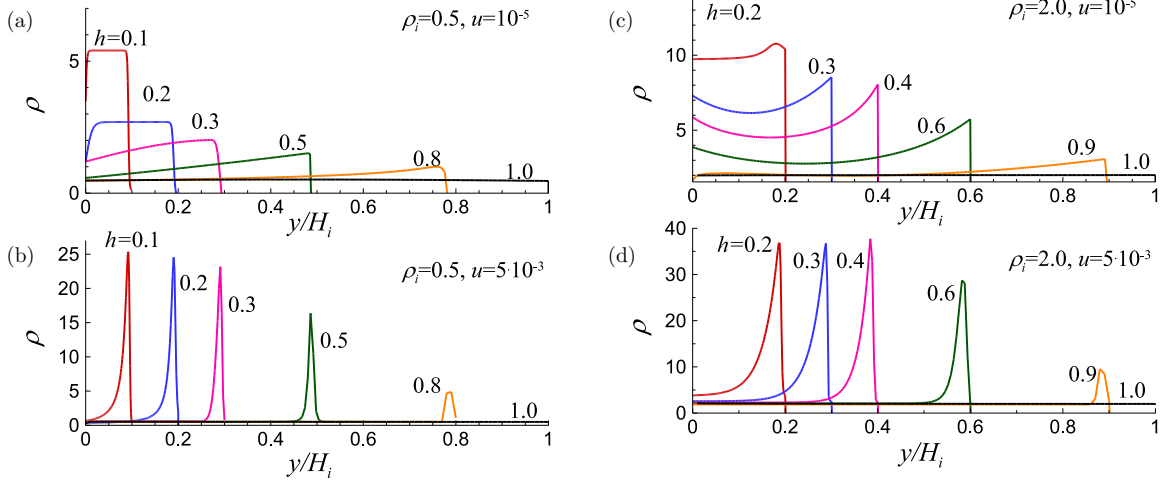


FIG. 4. Profiles of number density,  $\rho(y/H_i)$  at different values of relative height of the film,  $h$ , for initial number density  $\rho_i = 0.5$  and drying rate  $u = 10^{-5}$  (a),  $\rho_i = 0.5, u = 5 \times 10^{-3}$  (b),  $\rho_i = 2.0, u = 10^{-5}$  (c), and  $\rho_i = 2.0, u = 5 \times 10^{-3}$  (d).

a constant drying rate,  $u = 10^{-3}$  [ $\rho_c = \infty$  in Eq. (5)] (a) and of a variable drying rate [ $\rho_c = 7$  in Eq. (5)] (b) are presented. The initial number density was  $\rho_i = 1.0$ . Comparison of the data presented in Fig. 2 allows the following preliminary conclusion to be drawn. In both cases the formation of the surface crust is evident. However, for the constant drying rate,  $u = 10^{-3}$  this crust is very thin and has a high number density as compared with the corresponding characteristic for the variable drying rate. The quantitative differences in the drying behavior of the systems considered above are demonstrated in Fig. 3. For the variable drying rate, the function  $u(t_{MC})$  is highly nonlinear with the most considerable drop at high values of  $t_{MC}$  [Fig. 3(a)]. For both the constant and variable drying rates the relative height of the film,  $h$ , decreased while the average order parameters  $S$  increased in the course of the drying [Fig. 3(b)]. However, the kinetics were much slower for the variable drying rate, naturally reflecting a slowdown in the drying rate. In the

final stages of drying, the values of  $S$  tended to one, although the nematic order was relatively homogeneous only for the variable drying rate [Fig. 2(a)], whereas isotropic order in the bulk of the dried film was observed for the constant drying rate [Fig. 2(b)].

The relationship between the experimental drying rate  $u^r$  and the computational value,  $u$ , can be expressed as

$$u = u^r \frac{\Delta t_{MC}}{l_s} = u^r \frac{\alpha^2 \tau_B}{l_s}. \quad (6)$$

For example, using the data for water viscosity  $\eta = 8 \times 10^4$  Pa s, drying rate  $u^r = 3.76 \times 10^{-7}$  m/s at room temperature,  $T = 298$  K [49], and Eq. (3) with parameters  $\alpha = 1/20$

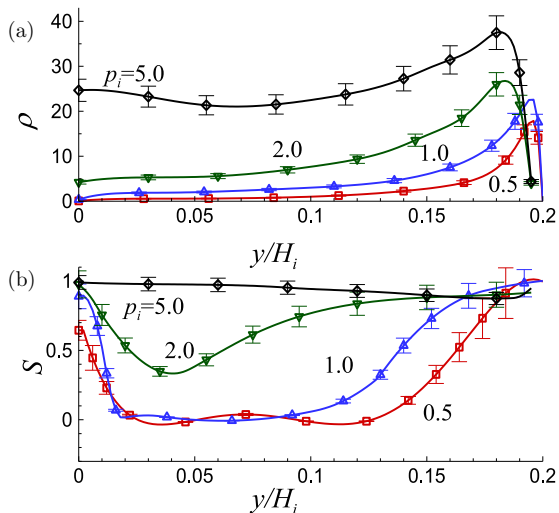


FIG. 5. Profiles of number density,  $\rho(y/H_i)$  (a), and local order parameter,  $S(y/H_i)$  (b), at different values of initial number density,  $\rho_i$ , at fixed value of the relative height of the film,  $h = 0.2$ , for the relatively high drying rate,  $u = 10^{-3}$ .

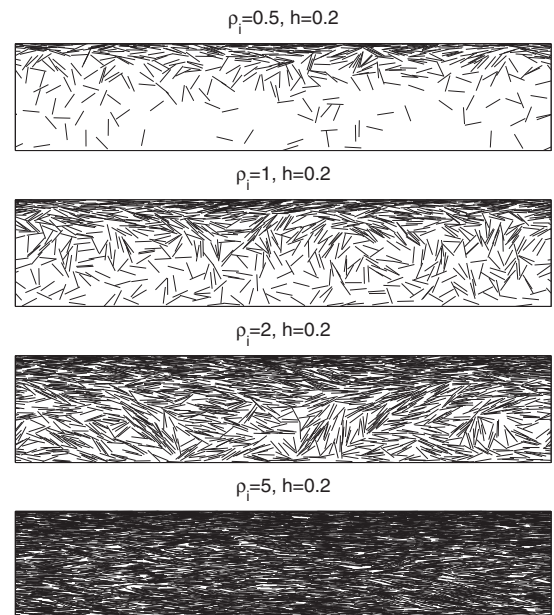


FIG. 6. Comparison of the drying patterns at different values of the initial number density,  $\rho_i$ , at a fixed value of the relative height of the film,  $h = 0.2$ , for the relatively high drying rate,  $u = 10^{-3}$ . See Ref. [50].

and  $k = 10^3$ , we can obtain  $u = 1.34 \times 10^{-3}$  for  $l_s = 5 \mu\text{m}$  and  $u = 5.37 \times 10^{-5}$  for  $l_s = 1 \mu\text{m}$ .

The Péclet number can be evaluated as

$$\text{Pe} = H_i^r u^r / D_t = \frac{4H_i}{\alpha^2} u, \quad (7)$$

where  $H_i^r = H_i l_s$  is the real initial height of the film. For  $H_i = 32$  as used in this work, we have  $\text{Pe} \approx 2.56 \times 10^3 u$ .

For each given value of  $\rho_i$  or  $u$ , the computer experiments were repeated 100 times, and then the data were averaged. The error bars in the figures correspond to the standard deviation of the mean. When not shown explicitly, they are of the order of the marker size.

### III. RESULTS AND DISCUSSION

Vertical drying processes were studied using drying rates,  $u$  in the interval between  $10^{-5}$  and  $5 \times 10^{-3}$ , that corresponded to the Péclet numbers in the interval between  $\approx 2.56 \times 10^{-2}$  and 12.8.

Figure 4 compares the profiles of number density,  $\rho(y)$ , for initial number density  $\rho_i = 0.5$  [at different drying rates,  $u = 10^{-5}$  ( $\text{Pe} \approx 2.56 \times 10^{-2}$ ) (a), and  $u = 5 \times 10^{-3}$  ( $\text{Pe} \approx 12.8$ ) (b)] and for  $\rho_i = 2.0$  [at  $u = 10^{-5}$  (c), and  $u = 5 \times 10^{-3}$  (d)]. The observed  $\rho(y)$  dependencies were rather different for drying modes with small and large Péclet numbers, and this was in qualitative correspondence with the previously discussed impact of the Péclet number on the spatial gradient in the density profiles [3]. For small Péclet numbers homogeneous density profiles inside the drying films were observed [Figs. 4(a) and 4(c)], whereas for large Péclet numbers peaks appeared near the upper interfaces [Figs. 4(b) and 4(d)] that obviously reflected the formation of crusts.

This conclusion is supported by the data on the profiles of the number density,  $\rho(y)$ , and local order parameter,  $S(y)$  [Figs. 5(a) and 5(b)]. Here the profiles are compared at different initial number densities,  $\rho_i$ , at the fixed value of the relative height of the dried film,  $h = 0.2$ , for a relatively high drying rate,  $u = 10^{-3}$ . The average number density at the given value of  $h$  can be evaluated as  $\rho = \rho_i / h$ . The corresponding patterns for different initial number densities,  $\rho_i$ , are presented in (Fig. 6). We see that at the highest value of  $\rho_i = 5$  insignificant densifications were observed near both the upper and bottom interfaces, while almost ideal ordering with  $S \approx 1$  was observed inside the dried film. At smaller initial densities, the densification (crust) and significant nematic ordering were observed only near the upper interface. Less significant orientational ordering was also observed near the bottom interface [Fig. 5(b)], and it decreased with decreasing values of  $\rho_i$ .

Figure 7 presents examples of the mean order parameter,  $S$ , versus the relative height of the film,  $h$ , at different drying rates,  $u$ , for initial number densities,  $\rho_i = 0.5$  (a), 1.0 (b), 2.0 (c), and 5.0 (d). Development of the drying process corresponds to the decrease in value of  $h$  and the increase in value of  $\rho$ .

The order parameter,  $S$ , always increased with increase of  $h$ . The observed  $S(h)$  dependencies were also rather different for drying modes with small and large Péclet numbers. At relatively small initial concentrations of sticks [ $\rho_i = 0.5$ ,  $\rho_i = 1.0$ , and  $\rho_i = 2.0$ , Figs. 7(a)–7(c)] an increase of  $u$  resulted in a

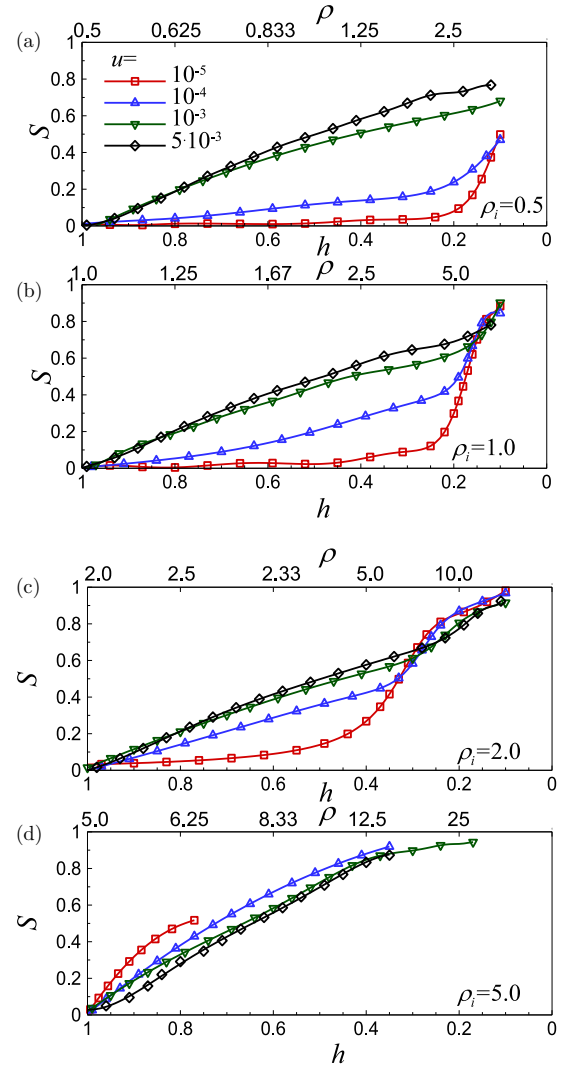


FIG. 7. Mean order parameter,  $S$ , versus the relative height of the film,  $h$ , at different drying rates,  $u$ , and initial number densities,  $\rho_i = 0.5$  (a), 1.0 (b), 2.0 (c), and 5.0 (d). The corresponding densities,  $\rho$ , are also presented on the upper horizontal axis.

more pronounced increase in the value of  $S$  with decreasing value of  $h$ .

For high evaporation rates,  $u = 5 \times 10^{-3}$  and  $u = 10^{-3}$ , a continuous increase in the value of  $S$  with decreasing value of  $h$  was observed, and this increase evidently reflected the formation of the crust layer near the vapor-liquid interface. For the small evaporation rates,  $u = 10^{-4}$  and  $u = 10^{-5}$ , a noticeable increase in the value of  $S$  was only observed in the final stages of drying. This could reflect the formation of dried layers with bulk ordering of the sticks. However, at the highest initial concentration of sticks [ $\rho_i = 5$ ; Fig. 7(d)] the opposite behavior was observed, and an increase of  $u$  resulted in a less pronounced increase in  $S$  with decreasing value of  $h$ . Such behavior could reflect the effects of bulk ordering at high concentrations of sticks.

Figure 8 presents examples of the electrical conductivity in the horizontal,  $\sigma_x$ , (a, c), and vertical,  $\sigma_y$ , (b, d), directions versus the relative height of the film,  $h$ . The initial density

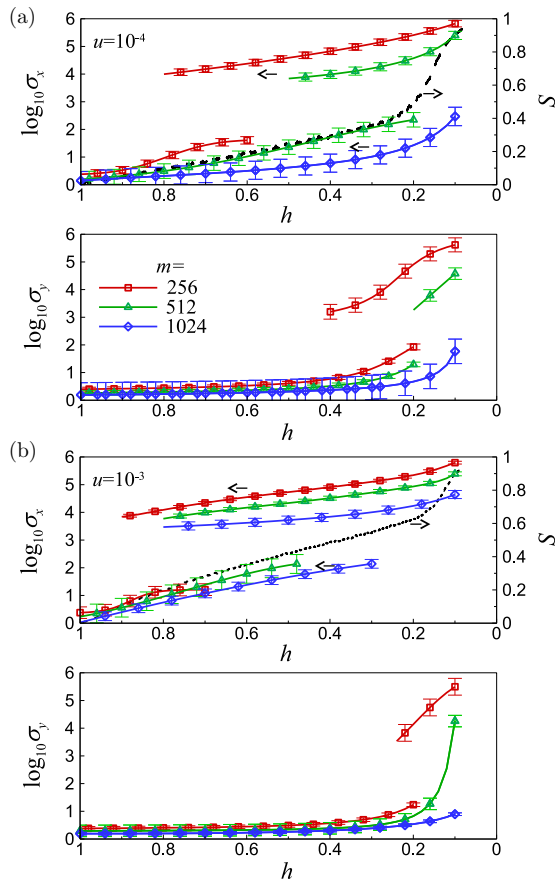


FIG. 8. Electrical conductivity in the horizontal,  $\sigma_x$ , and vertical,  $\sigma_y$ , directions versus the relative height of the film,  $h$ , at an initial density of  $\rho_i = 0.1$  and different drying rates,  $u = 10^{-4}$  (a) and  $u = 10^{-3}$  (b). The data are presented for different sizes of the supporting square lattice,  $m = 256, 512,$  and  $1024$ . The dashed lines correspond to the evolution of order parameter,  $S$ , during the drying.

was  $\rho_i = 0.1$  and different drying rates,  $u = 10^{-4}$  (a, b) and  $u = 10^{-3}$  (c, d), were considered. The data are presented for different sizes of the supporting square lattice,  $m = 256, 512,$  and  $1024$ . In fact, the use of the supporting square lattice for the calculation of electrical conductivity is equivalent to the rasterization of the structure of the infinitely thin sticks and substitution of them by the sticks with a finite aspect ratio of

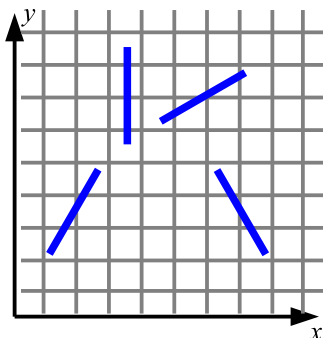


FIG. 9. Example of a supporting lattice.

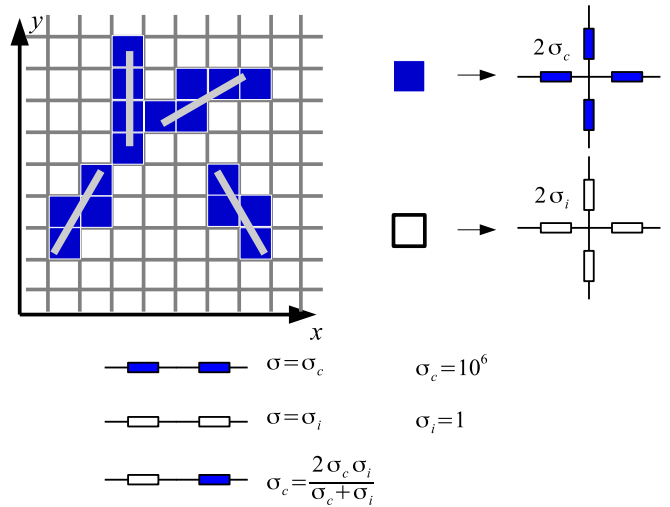


FIG. 10. Example of transformation of cells into sets of conductors.

the order of  $k \approx m/32$ . The system with infinitely thin sticks corresponds to that with very large values of  $m/32 \gg 1$ .

The values of  $\sigma_x$  and  $\sigma_y$  increased with decreasing value of  $h$  in the course of drying as this naturally reflects the changes in stick density in the film. Moreover, the calculated data pointed to the presence of significant anisotropy of electrical conductivity in the drying films with  $\sigma_x > \sigma_y$ . Such anisotropy clearly reflected the development of the preferential orientation of the sticks along the horizontal direction,  $x$ , during the drying [see the dashed lines in Fig. 8(a) and 8(b) for the dependency of the order parameter,  $S(h)$ ].

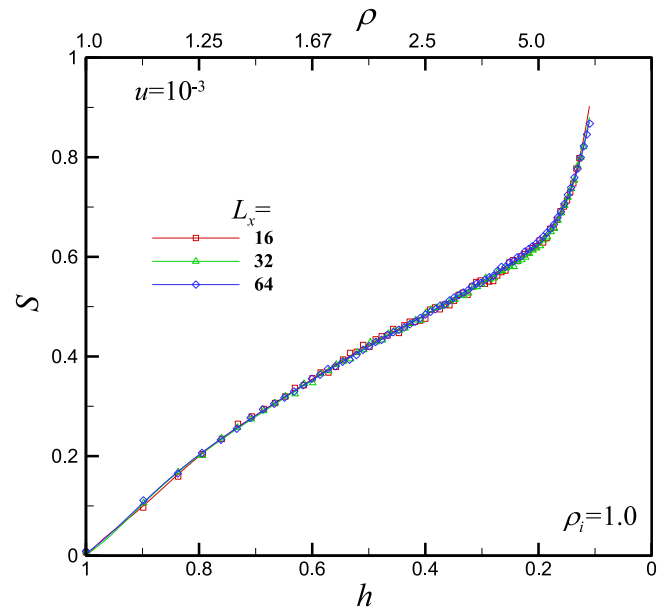


FIG. 11. Mean order parameter,  $S$ , versus the relative height of the film,  $h$ , at fixed drying rate  $u = 10^{-3}$  and initial number density  $\rho_i = 1.0$ . The corresponding densities,  $\rho$ , are also presented on the upper horizontal axis.

In some intervals of the  $h$  values the dependencies  $\sigma_x(h)$  and  $\sigma_y(h)$  can be continuous or discontinuous with two branches for the electrical conductivities. The upper and lower branches correspond to the formation and decomposition of percolation networks between the sticks. The effects of such a discontinuity were even more pronounced for a higher drying rate [Fig. 8(a)] as compared with the smaller one in Fig. 8(b). For example, for sticks with the large aspect ratio  $k = 16$  the discontinuities were not observed for  $u = 10^4$  and were observed for  $u = 10^{-3}$ . Such behavior may reflect the impact of the drying rate on the ordering of the sticks and the formation of the crust layer near the vapor-liquid interface at the high evaporation rate,  $u = 10^{-3}$  (i.e., at  $Pe \gg 1$ ).

#### IV. CONCLUSION

The continuous 2D model of the vertical drying of a suspension of infinitively thin sticks was studied by MC simulation. The initial homogeneous and isotropic state before drying was produced using the RSA model. As a result of evaporation, the upper interface moved down and the sticks underwent both translational and rotational Brownian motions. The restriction of evaporation due to the densification of the system near the upper interface was taken into account. The data revealed the presence of evaporation-driven and diffusion-driven self-assemblies and stratification of the sticks in the vertical direction. The sticks tend to orient along the horizontal direction in several layers close to both the upper (liquid-vapor) and bottom (liquid-solid wall) contact lines. The effects were dependent on the Péclet number and the initial number density. For small Péclet numbers, homogeneous density profiles inside the drying films were observed, whereas for large Péclet numbers, peaks appeared near the upper interfaces that evidently reflected the formation of crusts. The results obtained were in qualitative correspondence with the previously discussed impact of Péclet number on the spatial gradient in density profiles [3]. At small initial density ( $\rho_i = 0.5$ ), the densifications (crusts) were observed only near the upper boundary, but significant nematic orderings were still observed near both the upper and bottom boundaries. However, for dense systems ( $\rho_i = 5$ ), insignificant densifications were observed near both the upper and bottom interfaces, and

practically ideal ordering with  $S \approx 1$  was observed inside the film. Our data have demonstrated the presence of significant anisotropy of electrical conductivity in the drying films with  $\sigma_x > \sigma_y$ . Such anisotropy evidently reflects the development of a preferential orientation of sticks in the horizontal direction,  $x$ , during the drying. This anisotropy can be finely regulated by changing the Péclet number and initial number density. These results present an interesting possibility for prediction of the electrical conductivity of dried films, obtained by the drying of suspensions filled with highly anisotropic nanoparticles. Surely the presented 2D model for hard-core and identical sticks is oversimplified. Although, behavior of 3D systems is supposed to be similar to the predictions of our 2D model, consideration of such systems is extremely time-consuming. In future investigations it is desirable to treat the more realistic systems accounting for the interactions among the rodlike particles and their polydispersity.

#### ACKNOWLEDGMENTS

We acknowledge the funding from the National Academy of Sciences of Ukraine, Project No. 43/17-H (N.I.L., N.V.V.), and the Ministry of Education and Science of the Russian Federation, Project No. 3.959.2017/4.6 (Yu.Yu.T.).

#### APPENDIX A: SUPPORTING LATTICE

Each cell (a face of the lattice) is treated as conducting when any part of a stick is located inside such the cell (Fig. 9).

To transform the lattice into a RRN, each cell is associated with a set of conductors (Fig. 10).

All possible combinations of the conductivities are indicated in Fig. 10.

#### APPENDIX B: SCALING ANALYSIS

Example of scaling analysis for the mean order parameter,  $S$ , is presented in Fig. 11.

The computations were performed for three systems with the same initial height  $H_i = 32l_s$  but different widths ( $L_x = 16l_s, 32l_s, 64l_s$ ). The deviations of the results obtained for different systems do not exceed the statistical errors.

- 
- [1] Z. Zhou and X. S. Zhao, Flow-controlled vertical deposition method for the fabrication of photonic crystals, *Langmuir* **20**, 1524 (2004).
  - [2] H. Zheng and S. Ravaine, Bottom-up assembly and applications of photonic materials, *Crystals* **6**, 54 (2016).
  - [3] A. F. Routh, Drying of thin colloidal films, *Rep. Prog. Phys.* **76**, 046603 (2013).
  - [4] Z. Xu, L. Wang, F. Fang, Y. Fu, and Z. Yin, A review on colloidal self-assembly and their applications, *Curr. Nanosci.* **12**, 725 (2016).
  - [5] V. R. Dugyala and M. G. Basavaraj, Evaporation of sessile drops containing colloidal rods: Coffee-ring and order-disorder transition, *J. Phys. Chem. B* **119**, 3860 (2015).
  - [6] L. Hu, D. S. Hecht, and G. Gruner, Carbon nanotube thin films: fabrication, properties, and applications, *Chem. Rev.* **110**, 5790 (2010).
  - [7] Q. Liao, L. Chen, X. Qu, and X. Jin, Brownian dynamics simulation of film formation of mixed polymer latex in the water evaporation stage, *J. Colloid. Interf. Sci.* **227**, 84 (2000).
  - [8] Y. Reyes and Y. Duda, Modeling of drying in films of colloidal particles, *Langmuir* **21**, 7057 (2005).
  - [9] Y. Reyes, F. Vázquez, and Y. Duda, The simplest model of the latex film formation through evaporation deposition: Monte Carlo study, *Adv. Technol. Mater. Mater. Process.* **7**, 127 (2005).
  - [10] Y. Reyes, J. Campos-Terán, F. Vázquez, and Y. Duda, Properties of films obtained from aqueous polymer dispersions: Study of drying rate and particle polydispersity effects, *Model. Simul. Mater. Sci. Eng.* **15**, 355 (2007).
  - [11] A. Fortini, I. Martín-Fabiani, J. L. De La Haye, P.-Y. Dugas, M. Lansalot, F. D'Agosto, E. Bourgeat-Lami, J. L. Keddie, and



- R. P. Sear, Dynamic Stratification in Drying Films of Colloidal Mixtures, *Phys. Rev. Lett.* **116**, 118301 (2016).
- [12] A. Fortini and R. P. Sear, Stratification and size segregation of ternary and polydisperse colloidal suspensions during drying, *Langmuir* **33**, 4796 (2017).
- [13] Y. Kameya, Kinetic Monte Carlo simulation of nanoparticle film formation via nanocolloid drying, *J. Nanopart. Res.* **19**, 214 (2017).
- [14] A. Gromer, M. Nassar, F. Thalmann, P. Hébraud, and Y. Holl, Simulation of latex film formation using a cell model in real space: Vertical drying, *Langmuir* **31**, 10983 (2015).
- [15] N. I. Lebovka, N. V. Vygornitskii, V. A. Gigiberiya, and Y. Yu. Tarasevich, Monte Carlo simulation of evaporation driven self-assembly in suspension of colloidal rods, *Phys. Rev. E* **94**, 062803 (2016).
- [16] T. F. Middleton and D. J. Wales, Comparison of kinetic monte carlo and molecular dynamics simulations of diffusion in a model glass former, *J. Chem. Phys.* **120**, 8134 (2004).
- [17] L. Onsager, The effects of shape on the interaction of colloidal particles, *Ann. N. Y. Acad. Sci.* **51**, 627 (1949).
- [18] J. P. Straley, Third virial coefficient for the gas of long rods, *Mol. Cryst. Liq. Cryst.* **24**, 7 (1973).
- [19] H. N. W. Lekkerkerker, Ph. Coulon, R. Van Der Haegen, and R. Deblieck, On the isotropic-liquid crystal phase separation in a solution of rodlike particles of different lengths, *J. Chem. Phys.* **80**, 3427 (1984).
- [20] T. Odijk, Theory of lyotropic polymer liquid crystals, *Macromolecules* **19**, 2313 (1986).
- [21] G. J. Vroege and H. N. W. Lekkerkerker, Phase transitions in lyotropic colloidal and polymer liquid crystals, *Rep. Prog. Phys.* **55**, 1241 (1992).
- [22] R. F. Kayser and H. J. Raveché, Bifurcation in Onsager's model of the isotropic-nematic transition, *Phys. Rev. A* **17**, 2067 (1978).
- [23] J. Y. Denham, G. R. Luckhurst, C. Zannoni, and J. W. Lewis, Computer simulation studies of anisotropic systems, III. Two-dimensional nematic liquid crystals, *Mol. Cryst. Liq. Cryst.* **60**, 185 (1980).
- [24] D. Frenkel and R. Eppenga, Evidence for algebraic orientational order in a two-dimensional hard-core nematic, *Phys. Rev. A* **31**, 1776 (1985).
- [25] M. A. Bates and D. Frenkel, Phase behavior of two-dimensional hard rod fluids, *J. Chem. Phys.* **112**, 10034 (2000).
- [26] J. Vieillard-Baron, Phase transitions of the classical hard-ellipse system, *J. Chem. Phys.* **56**, 4729 (1972).
- [27] R. Hentschke, L. Askadskaya, and J. P. Rabe, A simple model for dense phases of two-dimensional hard rods and its application to mono- and bidisperse alkanes physisorbed on graphite, *J. Chem. Phys.* **97**, 6901 (1992).
- [28] P. van der Schoot, Nematics of linear assemblies in two dimensions, *J. Chem. Phys.* **106**, 2355 (1997).
- [29] H. H. Wensink and R. L. C. Vink, First-order phase transitions in two-dimensional off-lattice liquid crystals, *J. Phys.: Condens. Matter* **19**, 466109 (2007).
- [30] A. Ghosh and D. Dhar, On the orientational ordering of long rods on a lattice, *EPL (Europhys. Lett.)* **78**, 20003 (2007).
- [31] L. G. López, D. H. Linares, A. J. Ramirez-Pastor, and S. A. Cannas, Phase diagram of self-assembled rigid rods on two-dimensional lattices: Theory and Monte Carlo simulations, *J. Chem. Phys.* **133**, 134706 (2010).
- [32] I. Lončarević, M. Z. Jakšić, B. S. Vrhovac, and Lj. Budinski-Petković, Irreversible deposition of extended objects with diffusional relaxation on discrete substrates, *Eur. Phys. J. B* **73**, 439 (2010).
- [33] J. Kundu and R. Rajesh, Reentrant disordered phase in a system of repulsive rods on a Bethe-like lattice, *Phys. Rev. E* **88**, 012134 (2013).
- [34] J. Kundu, R. Rajesh, D. Dhar, and J. F. Stilck, Nematic-disordered phase transition in systems of long rigid rods on two-dimensional lattices, *Phys. Rev. E* **87**, 032103 (2013).
- [35] D. A. Matoz-Fernandez, D. H. Linares, and A. J. Ramirez-Pastor, Nonmonotonic size dependence of the critical concentration in 2D percolation of straight rigid rods under equilibrium conditions, *Eur. Phys. J. B* **85**, 1 (2012).
- [36] N. I. Lebovka, Y. Yu. Tarasevich, V. A. Gigiberiya, and N. V. Vygornitskii, Diffusion-driven self-assembly of rodlike particles: Monte Carlo simulation on a square lattice, *Phys. Rev. E* **95**, 052130 (2017).
- [37] J. W. Evans, Random and cooperative sequential adsorption, *Rev. Mod. Phys.* **65**, 1281 (1993).
- [38] J. D. Sherwood, Random sequential adsorption of lines and ellipses, *J. Phys. A: Math. Gen.* **23**, 2827 (1990).
- [39] R. D. Vigil and R. M. Ziff, Kinetics of random sequential adsorption of rectangles and line segments, *J. Chem. Phys.* **93**, 8270 (1990).
- [40] R. M. Ziff and R. D. Vigil, Kinetics and fractal properties of the random sequential adsorption of line segments, *J. Phys. A: Math. Gen.* **23**, 5103 (1990).
- [41] R. D. Vigil and R. M. Ziff, Random sequential adsorption of unoriented rectangles onto a plane, *J. Chem. Phys.* **91**, 2599 (1989).
- [42] G. Li and J. X. Tang, Diffusion of actin filaments within a thin layer between two walls, *Phys. Rev. E* **69**, 061921 (2004).
- [43] S. Broersma, Rotational diffusion constant of a cylindrical particle, *J. Chem. Phys.* **32**, 1626 (1960).
- [44] S. Broersma, Viscous force constant for a closed cylinder, *J. Chem. Phys.* **32**, 1632 (1960).
- [45] S. Broersma, Viscous force and torque constants for a cylinder, *J. Chem. Phys.* **74**, 6989 (1981).
- [46] D. P. Landau and K. Binder, *A Guide to Monte Carlo Simulations in Statistical Physics*, 4th ed. (Cambridge University Press, Cambridge, 2014).
- [47] D. J. Frank and C. J. Lobb, Highly efficient algorithm for percolative transport studies in two dimensions, *Phys. Rev. B* **37**, 302 (1988).
- [48] N. Lebovka, S. Khrapatiy, M. Vygornitskyi, and N. Pivovarova, Barrier properties of  $k$ -mer packings, *Physica A* **408**, 19 (2014).
- [49] D. G. Kröger and G. R. Branfield, Evaporation from a water surface: Theory and experiment, *R & D J.* **23**, 5 (2007).
- [50] See Supplemental Material at <http://link.aps.org/supplemental/10.1103/PhysRevE.97.022136> for animations of Figs. 6(b) and 6(d).